PAPER • OPEN ACCESS

Dynamical dimerization phase in Jaynes–Cummings lattices

View the article online for updates and enhancements.

New Journal of Physics

The open access journal at the forefront of physics

PAPER

CrossMark

Dynamical dimerization phase in Jaynes–Cummings lattices

Rubén Peña[1], Felipe Torres[2,3] and Guillermo Romero[1,3] ⓘ

[1] Departamento de Física, Universidad de Santiago de Chile (USACH), Avenida Ecuador 3493, 9170124, Santiago, Chile
[2] Departamento de Física, Facultad de Ciencias, Universidad de Chile, Casilla 653, Santiago, 7800024, Chile
[3] Center for the Development of Nanoscience and Nanotechnology, Estación Central, 9170124, Santiago, Chile

E-mail: guillermo.romero@usach.cl

Abstract

We report on an emergent dynamical phase of a strongly-correlated light–matter system, which is governed by dimerization processes due to short-range and long-range two-body interactions. The dynamical phase is characterized by the spontaneous symmetry breaking of the translational invariance and appears in an intermediate regime of light–matter interaction between the resonant and dispersive cases. We describe the quench dynamics from an initial state with integer filling factor of a finite-sized array of coupled resonators, each doped with a two-level system, in a closed and open scenario. The closed system dynamics has an effective Hilbert space description that allows us to demonstrate and characterize the emergent dynamical phase via time-averaged quantities, such as fluctuations in the number of polaritons per site and linear entropy. We prove that the dynamical phase is governed by intrinsic two-body interactions and the lattice topological structure. In the open system dynamics, we show evidence about the robustness of dynamical dimerization processes under loss mechanisms. Our findings can be used to determine the light–matter detuning range, where the dimerized phase emerges.

1. Introduction

The development of technology encompasses a broad range of opportunities to harness quantum phenomena. For instance, it is possible to manipulate light–matter quasiparticles or polaritons which have new properties such as stimulated scattering [1, 2], lasing [3–5], parametric amplification [6–8], and superfluidity [9, 10]. These characteristics can be used to enhance the experimental realization of polaritonic devices, such as semiconductor microcavities, where the coupling between quantum-well excitons and cavity photons gives rise to hybrid light–matter quasiparticles [11]. In the microwave regime, superconducting circuits based on Josephson junctions also allow us to harness light–matter interaction for simulating strongly correlated phenomena with light [12–22]. The underlying physics of light–matter based quantum simulators is governed by the Jaynes–Cummings–Hubbard (JCH) model [23–25] which describes the dynamics of coupled-resonator arrays (CRAs), each doped with a two-level system (TLS). In this case, the manipulation of polaritonic excitations locally depends on the detuning between the light and matter frequencies but also is largely influenced by the lattice structure. As the detuning increases from the resonant to the dispersive regime, the system transits from the Mott-insulating state characterized by the hybridization of light and matter states to a superfluid phase of photons [23–30].

In this work, we demonstrate by using numerical calculation and an analytic model that during the phase transition from the Mott-insulating to superfluid state, a dynamical dimerization phase (DDP) emerges, which is characterized by the spontaneous symmetry breaking of the translational invariance. As dynamical dimerization, we refer to the dynamics of a finite-sized Jaynes–Cummings (JC) lattice that exhibits resonances related to the two-sites JC lattice. In order to identify the new regime of DDP, we analyze the purely unitary quench dynamics of few-body JC lattices. In particular, we consider a quantum quench from an initial state with integer filling factor in a JC dimer, which has been proven useful to simulating second-order like phase
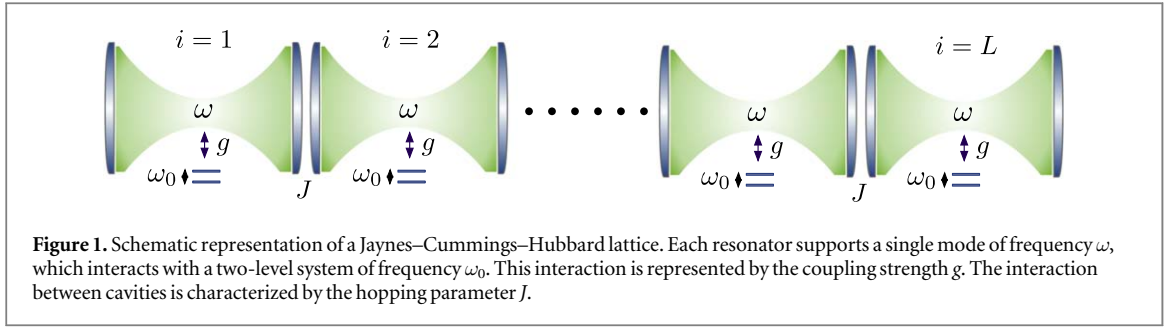
Figure 1. Schematic representation of a Jaynes–Cummings–Hubbard lattice. Each resonator supports a single mode of frequency ω, which interacts with a two-level system of frequency ω_0. This interaction is represented by the coupling strength g. The interaction between cavities is characterized by the hopping parameter J.

transitions from the Mott-insulating to superfluid phase [31]. Here, we introduce an effective Hilbert space in the two-excitations subspace using the criterion of discarding higher energy polaritonic states, which are out-of-resonance over the evolution [27, 32]. This description allows us quantitative explanations for time-averaged quantities such as fluctuations in the number of polaritons per site and linear entropy. Besides, the computational cost is substantially diminished by using a reduced effective Hilbert space. As we extend the quench dynamics to complex finite-sized CRAs, we demonstrate the emergence of DDP, which is governed by intrinsic two-body interactions in the JC lattice. In the open system scenario, our numerical results show evidence about the robustness of dynamical dimerization processes under loss mechanisms, so our work may find inspiration for the observation of DDP within state-of-the-art quantum technologies such as superconducting circuits [15, 17] and trapped ions [33, 34].

This paper is organized as follows. In section 2, we introduce the JCH model and the polariton mapping. In section 3, we describe the quench protocol for the closed JCH dimer. Here, we provide analytical expressions for time-averaged order parameters using an effective Hilbert space. In section 4, we highlight the emergence of a DDP as we extend the one-dimensional JC lattice to three and four sites. Here, section 4.1 describes DDP in a closed system, while in section 4.2, we introduce loss mechanisms in the JC lattice and discuss their effects on the dynamical phase transition. Finally, in section 5, we present our concluding remarks.

2. The model

The JCH model [23–25] describes a lattice of L interacting coupled QED resonators, each supporting a single mode of the electromagnetic field which interacts with a TLS. This situation is schematically shown in figure 1. The JCH Hamiltonian reads ($\hbar = 1$)

$$H_{\text{JCH}} = \sum_i H_i^{\text{JC}} - \sum_{\langle i,j \rangle} J_{ij}(a_i^\dagger a_j + a_j^\dagger a_i), \tag{1}$$

where $a_i(a_i^\dagger)$ is the annihilation (creation) bosonic operator at the ith lattice site, J_{ij} is the photon–photon hopping amplitude which takes values $J_{ij} = J$ if two sites of the lattice are connected and $J_{ij} = 0$ otherwise. Also, $H_i^{\text{JC}} = \omega a_i^\dagger a_i + \omega_0 \sigma_i^+ \sigma_i^- + g(\sigma_i^+ a_i + \sigma_i^- a_i^\dagger)$ is the JC Hamiltonian [35] where $\sigma_i^+ (\sigma_i^-)$ is the raising (lowering) operator acting on the ith TLS eigenbasis $\{|\downarrow\rangle_i, |\uparrow\rangle_i\}$, and ω, ω_0, and g are the resonator frequency, TLS frequency, and light–matter coupling strength, respectively.

In the resonant regime, $\Delta = \omega_0 - \omega = 0$, the hybridization of the light–matter yields to localized polariton excitations (Mott-insulator phase), while in the dispersive regime, $\Delta \gg g$, the system is dominated by photonic excitation behavior (superfluid phase) [23, 24]. This phase transition can also be described as a transition driven by the photon blockade effect from the Mott-insulator phase, where the intersite polariton exchange is forbidden, so effectively $J_{ij} = 0$, to a superfluid phase dominated by a uniform photon hopping $J_{ij} = J$, in both cases, there is no cavity-embedded effect involved. As we demonstrate in section 4, the intermediate regime of light–matter interaction, which we define in the range $1 < \Delta/g < 10$, can be identified by the parameter $k_i = J(\sum_j \nu_j)/L$ with L the number of nonlinear coupled resonators, J the hopping parameter, and ν_j the connectivity of node j. Notice that $k_i = 0$ for the resonant case and $k_i = J$ for the dispersive case. This way, the origin of translational symmetry breaking can be explained by introducing a local order parameter of μth phase Ψ_i^μ, with $\mu = (\text{I, II, III})$ represents the resonant, intermediate, and dispersive case, respectively. Indeed, $\Psi_i^{\text{I}}(k_i) = \Psi^{\text{I}}(0)$, and $\Psi_i^{\text{III}}(k_i) = \Psi^{\text{III}}(J)$, which means that in the resonant and dispersive regimes there is translational invariance. Since the order parameter shows a spatial dependence in an intermediate regime $\Psi_i^{\text{II}}(k_i)$, then translational symmetry is broken. As a consequence, a DDP will happen due to intrinsic two-body interactions and the connectivity of each lattice site.

The Hamiltonian (1) preserves the total number excitations (polaritons) described by the operator $\mathcal{N} = \sum_{i=1}^L (a_i^\dagger a_i + \sigma_i^+ \sigma_i^-)$. The ith node of the lattice in figure 1 is described by the JC Hamiltonian H_i^{JC} whose eigenstates define the upper (+) and lower (−) polaritonic basis $|n, \pm\rangle_i = \gamma_{n\pm}|\downarrow, n\rangle_i + \rho_{n\pm}|\uparrow, n-1\rangle_i$ with

energies $E_n^\pm = n\omega + \Delta/2 \pm \chi(n)$. Here, $\chi(n) = \sqrt{\Delta^2/4 + g^2 n}$, $\rho_{n+} = \cos(\theta_n/2)$, $\gamma_{n+} = \sin(\theta_n/2)$, $\rho_{n-} = -\gamma_{n+}$, $\gamma_{n-} = \rho_{n+}$, $\tan\theta_n = 2g\sqrt{n}/\Delta$, and the detuning parameter $\Delta = \omega_0 - \omega$. Also, one introduces the ith polaritonic creation operators as $P_i^{\dagger(n,\alpha)} = |n,\alpha\rangle_i\langle 0,-|$, where $\alpha = \pm$ and we identify $|0,-\rangle \equiv |\downarrow,0\rangle$ and $|0,+\rangle \equiv |\varnothing\rangle$ being a ket with all entries equal to zero, that is, it represents an unphysical state. These identifications imply $\gamma_{0-} = 1$ and $\gamma_{0+} = \rho_{0\pm} = 0$.

Using the above defined polaritonic basis, the Hamiltonian (1) can be rewritten as [23, 27]

$$H = \sum_{i=1}^{L}\sum_{n=1}^{\infty}\sum_{\alpha=\pm} E_n^\alpha P_i^{\dagger(n,\alpha)} P_i^{(n,\alpha)} - \sum_{\langle i,j \rangle} J_{ij}\left[\sum_{n,m=1}^{\infty}\sum_{\alpha,\alpha',\beta,\beta'=\pm} t_n^{\alpha\alpha'} t_m^{\beta\beta'} P_i^{\dagger(n-1,\alpha)} P_i^{(n,\alpha')} P_j^{\dagger(m,\beta)} P_j^{(m-1,\beta')} + \text{h.c} \right], \quad (2)$$

where the matrix elements $t_n^{\alpha\alpha'} = \sqrt{n}\,\gamma_{(n-1)\alpha}\gamma_{n\alpha'} + \sqrt{n-1}\,\rho_{(n-1)\alpha}\rho_{n\alpha'}$. The first term in equation (2) stands for the local polaritonic energy with an anharmonic spectrum and gives rise to an effective on-site polaritonic repulsion. This is analog to the on-site photon repulsion in the Bose–Hubbard model [36]. The last term in equation (2) represents the polariton hopping between resonators. This interaction also allows the interchange of polaritonic species of one or both sites involved [23, 27, 32], leading to a quite involve quantum dynamics.

A detailed understanding of the equilibrium properties of the JCH model (2) resorts on approximated analytical solutions [37] or numerical approaches such as density matrix renormalization group [38–41]. In nonequilibrium situations, one can understand the underlying physics using the time-evolving block decimation algorithm [42–44], or simplifying the description using effective Hilbert spaces [32, 45–49]. The latter is particularly appropriate for studying the quench protocol presented in this article, as we consider the closed system scenario.

3. Quench dynamics in a JCH dimer

In this section, we introduce a sudden quench protocol [31] and its effects on the quantum dynamics of the JCH dimer. Also, we provide quantitative explanations of time-averaged quantities such as fluctuations in the number of polaritons per site and linear entropy using an effective Hilbert space. In section 4, we will show that the underlying physics of the quench dynamics allows us to understand the emergent DDP. We stress that DDP occurring in the JCH lattice happens in the frequency regime $Jn \ll g\sqrt{n} \ll \omega n$ [23], where the rotating wave approximation holds.

For each detuning Δ, we set the initial condition as the lowest energy state with integer filling factor of one excitation per site, that is, $|\psi_0\rangle = \bigotimes_{i=1}^{L}|1,-\rangle_i$ (L is the number of lattice sites) which corresponds to a Mott-insulating state at hopping rate $J = 0$. Then, at time $t = 0$, the parameter J is suddenly quench to a new value $J_f \neq 0$ such that the Hamiltonian has changed to $H = H_{\text{JCH}}(J_f)$. Hence, the JCH lattice dynamics is described by the state $|\psi_0(t)\rangle = e^{-iHt}|\psi_0\rangle$ ($\hbar = 1$) which leads to nonequilibrium phenomena. In order to characterize DDP, we compute time-averaged order parameters such as the variance of the number of polaritons per site $\text{Var}(n_i) = \frac{1}{\tau}\int_0^\tau dt\,(\langle n_i^2\rangle - \langle n_i\rangle^2)$, where $n_i = a_i^\dagger a_i + \sigma_i^+\sigma_i^-$, and $\tau = J^{-1}$, or the linear entropy $E = \frac{1}{\tau}\int_0^\tau dt\,S_{\rho_i}(t)$, where $S_{\rho_i}(t) = 1 - \text{Tr}(\rho_i^2)$, and ρ_i the reduced density matrix of the leftmost or rightmost site of the JC dimer.

The quench protocol described above allows us to simulating second-order like phase transition captured via the $\text{Var}(n_i)$, see [31], which is analog to the adiabatic dynamics studied in [23]. Also, the simulated phase transitions in a JCH lattice can be characterized via linear entropy, as shown in this article, which implies that the observation of the emergent DDP is independent of the choice of the order parameter.

Effective Hilbert space for a closed system.—In order to introduce an effective description of the system dynamics, it is useful to consider the JCH Hamiltonian written in the polaritonic basis, see equation (2). Starting from the initial state $|\psi_0\rangle = |1,-\rangle_i|1,-\rangle_j$, the JCH Hamiltonian (2) may lead to processes such as the exchange of polaritonic species, or the interchange of polaritonic species of one or both sites involved (i,j). In this case, the full quantum dynamics should involve all states within the two-excitations subspace, which we define as $\{|\psi_0\rangle = |1,-\rangle_i|1,-\rangle_j, |\psi_2^\pm\rangle_i = |2,\pm\rangle_i|0,-\rangle_j, |\psi_2^\pm\rangle_j = |0,-\rangle_i|2,\pm\rangle_j, |\psi_1^+\rangle_i = |1,+\rangle_i|1,-\rangle_j, |\psi_1^+\rangle_j = |1,-\rangle_i|1,+\rangle_j, |\psi_1^+\rangle_{ij} = |1,+\rangle_i|1,+\rangle_j\}$. However, interchange of polaritonic excitations can be neglected under the conditions $\{|E_2^+ - 2E_1^-|, |2E_1^+ - E_2^-|, |E_1^+ + E_1^- - E_2^-|\} \gg J$, which results in fast oscillating contributions, and we can apply the rotating-wave approximation [23, 27, 32]. Figure 2 shows that the interchange of polaritonic species is suppressed over the evolution. Here we plot the populations of above defined states as a function of time. We identify populations as $P_0 = |\langle\psi_0|\psi(t)\rangle|^2$, $P_{2i}^\pm = |_i\langle\psi_2^\pm|\psi(t)\rangle|^2$, $P_{1i}^+ = |_i\langle\psi_1^+|\psi(t)\rangle|^2$, and $P_{ij}^+ = |_{ij}\langle\psi_1^+|\psi(t)\rangle|^2$. Due to the symmetry of the JC dimer, it is cleat that $P_{2j}^\pm = |_j\langle\psi_2^\pm|\psi(t)\rangle|^2 = P_{2i}^\pm$ and $P_{1j}^+ = |_j\langle\psi_1^+|\psi(t)\rangle|^2 = P_{1i}^+$ (not shown in figure 2). In this work, we carry out numerical calculations with the quantum toolbox in Python QuTiP [50, 51].
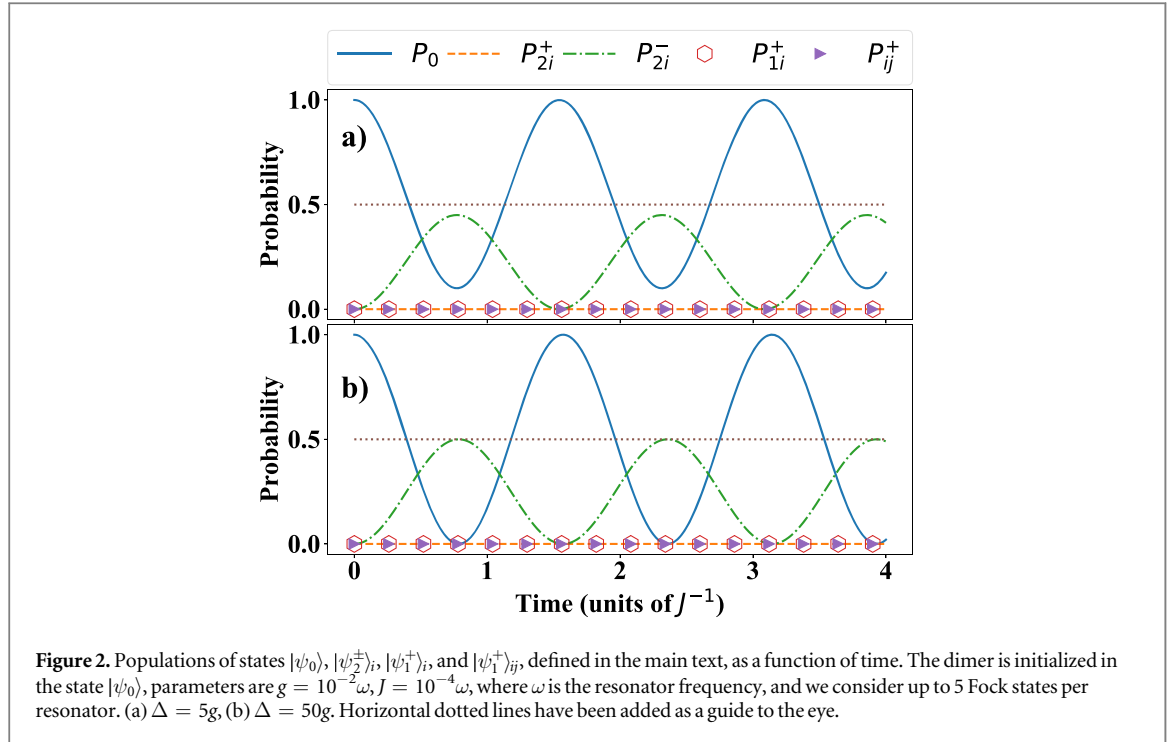
Figure 2. Populations of states $|\psi_0\rangle$, $|\psi_2^\pm\rangle_i$, $|\psi_1^+\rangle_i$, and $|\psi_1^+\rangle_{ij}$, defined in the main text, as a function of time. The dimer is initialized in the state $|\psi_0\rangle$, parameters are $g = 10^{-2}\omega$, $J = 10^{-4}\omega$, where ω is the resonator frequency, and we consider up to 5 Fock states per resonator. (a) $\Delta = 5g$, (b) $\Delta = 50g$. Horizontal dotted lines have been added as a guide to the eye.

Since the interchange of polaritonic species is suppressed over the evolution, we can introduce an effective Hilbert space involving states of the lower polaritonic branch $\mathcal{H}_I = \{|\psi_0\rangle, |\psi_2^-\rangle_i, |\psi_2^-\rangle_j\}$ for describing the quench dynamics. In this case, the effective Hamiltonian reads ($\hbar = 1$)

$$H_{\text{eff}} = \begin{pmatrix} a & b & b \\ b & c & 0 \\ b & 0 & c \end{pmatrix}, \tag{3}$$

where $a = 2E_1^-$, $b = -Jt_1^{--}t_2^{--}$, $c = E_2^-$, and $t_1^{--}t_2^{--} = \cos(\theta_1/2)(\sqrt{2}\,\cos(\theta_1/2)\cos(\theta_2/2) + \sin(\theta_1/2)\sin(\theta_2/2))$. Thus, the full dynamics can be solved analytically by diagonalizing the above 3×3 matrix.

Starting from the initial condition $|\psi_0\rangle = |1, -\rangle_i|1, -\rangle_j$, the wave function at time *t* reads

$$|\psi(t)\rangle = c_0(t)|\psi_0\rangle + c_{2i}^-(t)|\psi_2^-\rangle_i + c_{2j}^-(t)|\psi_2^-\rangle_j, \tag{4}$$

where the probability amplitudes are

$$c_0(t) = \frac{1}{\alpha_+ - \alpha_-}(\alpha_+ e^{-it\lambda_+} - \alpha_- e^{-it\lambda_-}), \tag{5a}$$

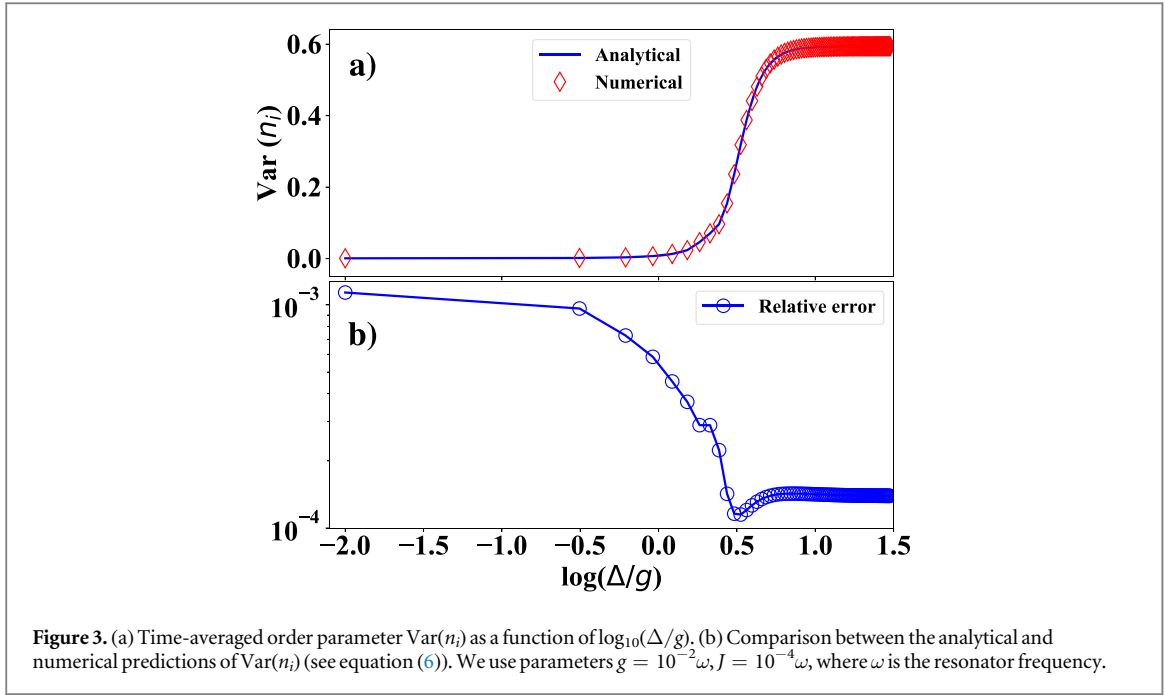$$c_{2i}^-(t) = c_{2j}^-(t) = \frac{1}{\alpha_+ - \alpha_-}(e^{-it\lambda_+} - e^{-it\lambda_-}), \tag{5b}$$

and we define the coefficients $\lambda_\pm = \left(a + c \pm \sqrt{8b^2 + (a - c)^2}\right)/2$, $\alpha_\pm = \left(a - c \pm \sqrt{8b^2 + (a - c)^2}\right)/2b$.

Time-averaged order parameters.—Given the wave function (4), we can analytically compute time-averaged order parameters such as the variance of the number of polaritons per site $\text{Var}(n_i) = \frac{1}{\tau}\int_0^\tau (\langle n_i^2 \rangle - \langle n_i \rangle^2)\mathrm{d}t$, where $n_i = a_i^\dagger a_i + \sigma_i^+\sigma_i^-$, or the linear entropy $E = \frac{1}{\tau}\int_0^\tau S_{\rho_i}(t)\mathrm{d}t$, where $S_{\rho_i}(t) = 1 - \text{Tr}(\rho_i^2)$, and ρ_i the reduced density matrix of the leftmost or rightmost site of the JC dimer. Thus, the time-averaged variance reads

$$\text{Var}(n_i) = \frac{4b^2}{\Omega_0^2}\left[1 - \frac{J}{\Omega_0}\sin\left(\frac{\Omega_0}{J}\right)\right], \tag{6}$$

where we define $\Omega_0 = \sqrt{8b^2 + (a - c)^2}$.

Figure 3(a) shows the behavior of $\text{Var}(n_i)$ as a function of $\log_{10}(\Delta/g)$ calculated from the full numerics (red diamonds) and the analytical prediction (continuous blue line) in equation (6). We see a good agreement between both predictions as the relative error shows in figure 3(b). Also, equation (6) allows us to predict the asymptotic behavior of $\text{Var}(n_i)$ as the detuning increases, $\Delta/g \to \infty$. In this case, the spectrum of the lower (upper) polaritonic branch becomes harmonic with eigenenergies $E_n^- \approx n\omega_R$ ($E_n^+ \approx n\omega_R + \Delta$), where $\omega_R = \omega - g^2/\Delta$, thus allowing the resonance condition $E_2^- - 2E_1^- = 0$ ($a = c$) (see figure 2(b)). Also, $|b| = \sqrt{2}J$ and $\Omega_0 = 4J$, so the asymptotic value of $\text{Var}(n_i)$ reads

Figure 3. (a) Time-averaged order parameter Var(n_i) as a function of $\log_{10}(\Delta/g)$. (b) Comparison between the analytical and numerical predictions of Var(n_i) (see equation (6)). We use parameters $g = 10^{-2}\omega$, $J = 10^{-4}\omega$, where ω is the resonator frequency.

$$\lim_{\Delta/g\to\infty} \mathrm{Var}(n_i) = \frac{1}{2}\left(1 - \frac{1}{4}\sin 4\right) = 0.5946. \tag{7}$$

It is worth mentioning that the analytical result (6) represents the hallmark for the dimer dynamics. In section 4, we will prove that as one increases the number of lattice sites, the time-averaged variance (6) allows us to identify resonances due to intrinsic short- and long-range two-body interactions, which govern the DDP.

On the other hand, one can also characterize the dimer dynamics via the linear entropy of the reduced density matrix as mixedness measure [52]. First, notice that the quantum state (4) is already in its Schmidt decomposition, which leads to a diagonal reduced density matrix

$$\rho_i = \begin{pmatrix} |c_{2j}^-(t)|^2 & 0 & 0 \\ 0 & |c_0(t)|^2 & 0 \\ 0 & 0 & |c_{2i}^-(t)|^2 \end{pmatrix}. \tag{8}$$

In this case, the linear entropy as a function of time is given by $S_{\rho_i}(t) = 1 - (|c_0(t)|^4 + 2|c_{2i}^-(t)|^4)$, and the time-averaged linear entropy reads

$$E = \frac{2b^2}{\Omega_0^5}\left[2\Omega_0\Omega_1^2 - 4J\Omega_2^2\sin\left(\frac{\Omega_0}{J}\right) - 3b^2J\sin\left(\frac{2\Omega_0}{J}\right)\right], \tag{9}$$

where $\Omega_1 = \sqrt{7b^2 + 2(a - c)^2}$ and $\Omega_2 = \sqrt{2b^2 + (a - c)^2}$. Figure 4(a) shows the behavior of E as a function of $\log_{10}(\Delta/g)$ calculated from the full numerics (red diamonds) and the analytical prediction (continuous blue line) in equation (9). We see a good agreement between analytical and numerical predictions as shown in figure 4(b). We can also estimate the asymptotic value of the time-averaged entropy as one increases the ratio Δ/g, it reads

$$\lim_{\Delta/g\to\infty} E = 0.4616. \tag{10}$$

In what follows, we will use the time-averaged variance (6) for demonstrating the existence of DDP in the intermediate regime of light–matter interaction. This choice establishes the physical framework for the subsequent discussion, but a similar analysis with the linear entropy leads to the same conclusion about DDP.

4. Dynamical dimerization phase

4.1. Closed system
Emergent dynamical critical phenomena following a quantum quench have experienced much interest in recent years [53–75]. Here, we demonstrate an emergent DDP as we extend the JC lattice to three (trimer) and four (tetramer) sites (see figure 1), and in an intermediate regime of light–matter coupling strength, that is, $1 < \Delta/g < 10$. We define the concept of dimerization as the dynamical process where short-range and long-range

Figure 4. (a) Time-averaged linear entropy E as a function of $\log_{10}(\Delta/g)$. (b) Comparison between the analytical and numerical predictions of E (see equation (9)). We use parameters $g = 10^{-2}\omega$, $J = 10^{-4}\omega$, where ω is the resonator frequency.
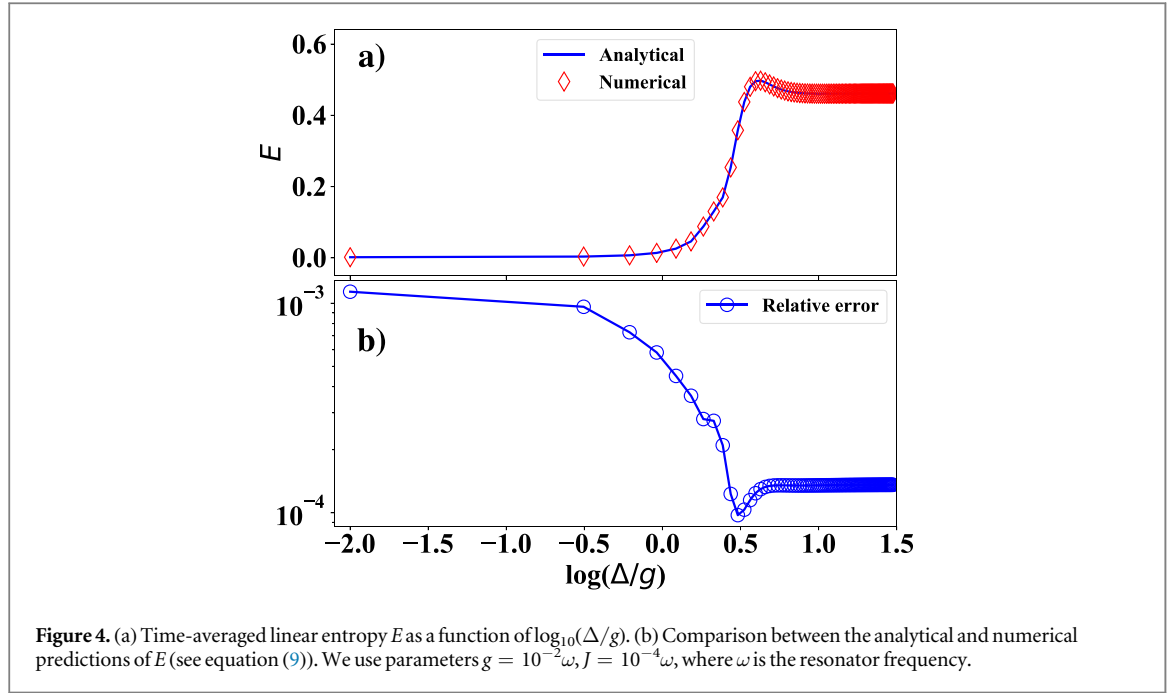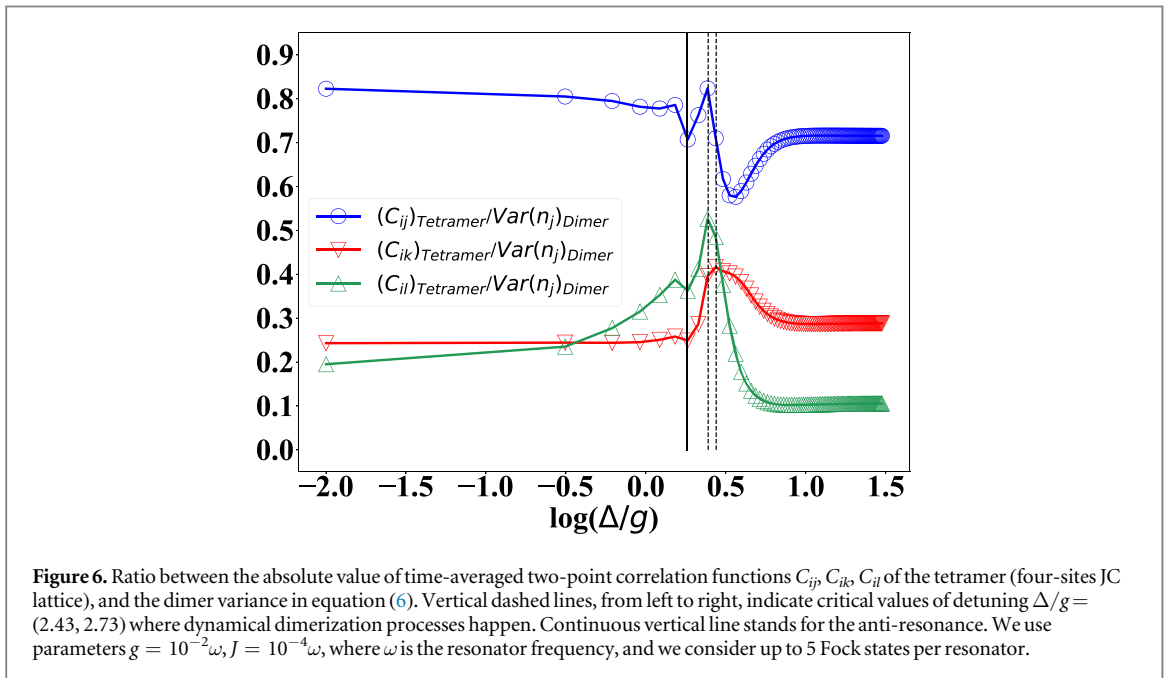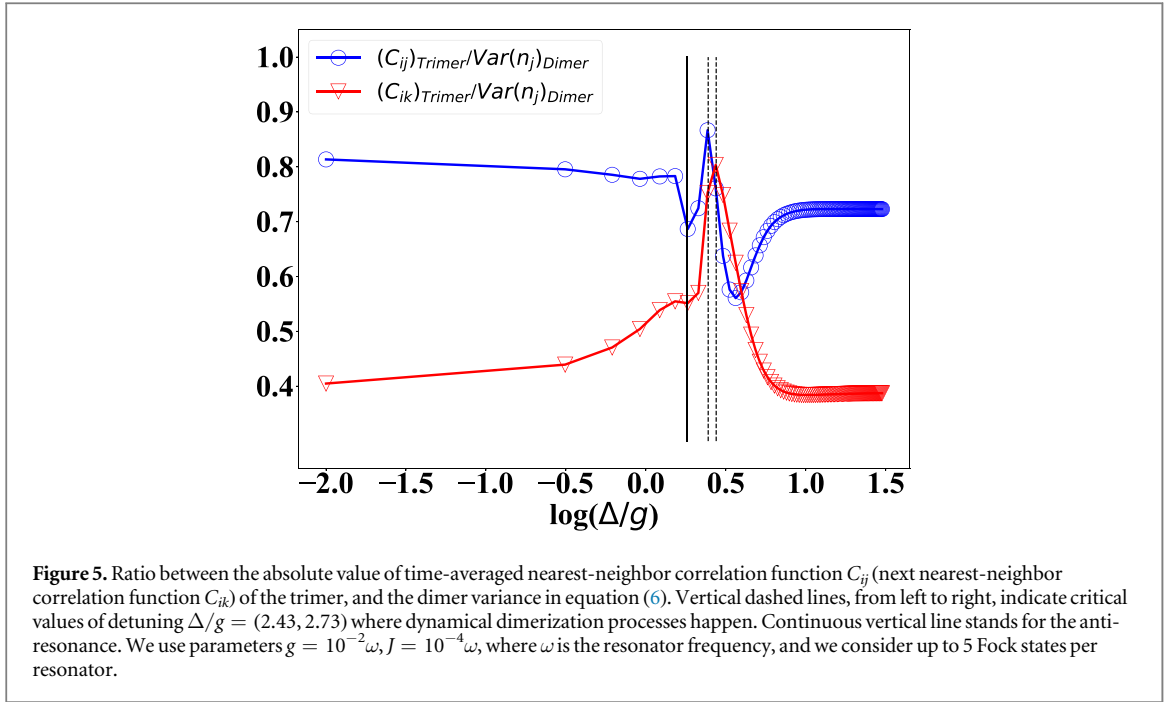
two-body interactions govern the quantum dynamics. Here, short-range (long-range) two-body interaction is due to the direct (mediated) exchange of polaritons. We will prove that the connectivity associated with each node of the lattice plays a crucial role to define DDP.

Let us start the discussion with a three-sites JC lattice initialized in the state $|\psi_0\rangle = |1, -\rangle_i|1, -\rangle_j|1, -\rangle_k$, where the subindexes i, j, and k refer to the leftmost, center, and rightmost lattice site, respectively. If we let the system evolves according to the quantum quench described is section 3, one should impose the conditions for neglecting interchange of polaritonic species between nearest-neighbor sites, that is, $\{|E_2^+ - 2E_1^-|, |2E_1^+ - E_2^-|, |E_1^+ + E_1^- - E_2^-|, |E_1^+ - E_1^-|, |E_3^+ - E_2^- - E_1^-|, |E_2^+ - E_2^-|, |E_2^+ + E_1^+ - E_2^- - E_1^-|\} \gg J$. As for the dimer, only the lower polaritonic branch will be activated and the dimension of the effective Hilbert space ($\mathcal{H}$) is given by $(N + d - 1)!/N!(d - 1)!$, where N is the number of excitations that should be distributed into d lattice sites. In our case, $N = 3$ and $d = 3$ results in $\dim(\mathcal{H}) = 10$. At time t, the wave function may be written as a linear combination of states belonging to the three-excitations subspace, that is

$$
\begin{aligned}
|\psi(t)\rangle = c_0(t)|\psi_0\rangle &+ c_{3j}|\psi_{3j}\rangle \\
&+ c_{3i}(t)(|\psi_{3i}\rangle + |\psi_{3k}\rangle) \\
&+ c_{2i1j}(t)(|\psi_{2i1j}\rangle + |\psi_{1j2k}\rangle) \\
&+ c_{1i2j}(t)(|\psi_{1i2j}\rangle + |\psi_{2j1k}\rangle) \\
&+ c_{2i1k}(t)(|\psi_{2i1k}\rangle + |\psi_{1i2k}\rangle),
\end{aligned}
\tag{11}
$$

where we define states $|\psi_0\rangle = |1, -\rangle_i|1, -\rangle_j|1, -\rangle_k$, $|\psi_{3i}\rangle = |3, -\rangle_i|0, -\rangle_j|0, -\rangle_k$, $|\psi_{3j}\rangle = |0, -\rangle_i|3, -\rangle_j|0, -\rangle_k$, $|\psi_{3k}\rangle = |0, -\rangle_i|0, -\rangle_j|3, -\rangle_k$, $|\psi_{2i1j}\rangle = |2, -\rangle_i|1, -\rangle_j|0, -\rangle_k$, $|\psi_{1j2k}\rangle = |0, -\rangle_i|1, -\rangle_j|2, -\rangle_k$, $|\psi_{1i2j}\rangle = |1, -\rangle_i|2, -\rangle_j|0, -\rangle_k$, $|\psi_{2j1k}\rangle = |0, -\rangle_i|2, -\rangle_j|1, -\rangle_k$, $|\psi_{2i1k}\rangle = |2, -\rangle_i|0, -\rangle_j|1, -\rangle_k$, and $|\psi_{1i2k}\rangle = |1, -\rangle_i|0, -\rangle_j|2, -\rangle_k$. Notice that some probability amplitudes are equal due to symmetry of the trimer with respect to the lattice center (j). Here, the state (11) will be computed via full numerics.

Figure 5 shows the ratio between the absolute value of the time-averaged nearest-neighbor correlation function C_{ij} (next nearest-neighbor correlation function C_{ik}) of the trimer, and the dimer variance (6). Two-point correlation functions are $C_{ij(k)} = \frac{1}{\tau}\int_0^\tau \mathrm{d}t\,(\langle n_i n_{j(k)}\rangle - \langle n_i\rangle\langle n_{j(k)}\rangle)$, where $\tau = J^{-1}$. Here, we identify two critical values of detuning, vertical dashed lines, $\Delta/g = (2.43, 2.73)$ within the intermediate regime of light–matter interaction, $1 < \Delta/g < 10$. At these critical points the trimer experiences dynamical dimerization processes, where short-range correlations rule the dynamics at $\Delta/g = 2.43$, while at $\Delta/g = 2.73$ a combination of both short- and long-range correlations govern the dynamics. The resonances shown in figure 5 demonstrate that the intrinsic dimer dynamics, characterized by the time-averaged variance (6), governs the quench dynamics of the trimer. Furthermore, the dimer variance allows us to identify short-range and long-range two-body interactions. The former is a consequence of direct cavity-cavity coupling of sites (i, k), while the latter results from an indirect interaction between sites (i, k) mediated by the center lattice site j. Notice that figure 5 also exhibits an anti-resonance at $\Delta = 1.82g$ (continuous vertical line). At this point, no dynamical dimerization happens, and the JC lattice remains approximately in the Mott insulating state.

Figure 5. Ratio between the absolute value of time-averaged nearest-neighbor correlation function C_{ij} (next nearest-neighbor correlation function C_{ik}) of the trimer, and the dimer variance in equation (6). Vertical dashed lines, from left to right, indicate critical values of detuning $\Delta/g = (2.43, 2.73)$ where dynamical dimerization processes happen. Continuous vertical line stands for the anti-resonance. We use parameters $g = 10^{-2}\omega, J = 10^{-4}\omega$, where ω is the resonator frequency, and we consider up to 5 Fock states per resonator.

Figure 6. Ratio between the absolute value of time-averaged two-point correlation functions C_{ij}, C_{ik}, C_{il} of the tetramer (four-sites JC lattice), and the dimer variance in equation (6). Vertical dashed lines, from left to right, indicate critical values of detuning $\Delta/g = (2.43, 2.73)$ where dynamical dimerization processes happen. Continuous vertical line stands for the anti-resonance. We use parameters $g = 10^{-2}\omega, J = 10^{-4}\omega$, where ω is the resonator frequency, and we consider up to 5 Fock states per resonator.

Let us discuss the results for the tetramer. Figure 6 shows the ratio between the absolute value of time-averaged two-point correlation functions C_{ij}, C_{ik}, C_{il} of the tetramer, and the dimer variance in equation (6). We order the lattice sites from left to the right according to indexes (i, j, k, l). It is noticeable that a larger JC lattice also exhibits resonances at critical values of detuning $\Delta/g = (2.43, 2.73)$ (vertical dashed lines), and the anti-resonance at $\Delta = 1.82g$ (continuous vertical line). Moreover, the two-point correlation function C_{il}, associated with edges of the lattice, has the same resonance ($\Delta = 2.43g$) as compared with nearest-neighbor correlation function C_{ij}. The latter suggests that for a finite one-dimensional JC lattice of L sites, the number of resonances associated with dimerization processes corresponds to a universal number of different connectivities of the lattice, that is, connectivity $\nu = 1$ for lattice edges, and connectivity $\nu = 2$ for bulk lattice sites. These results are a consequence of the broken translational symmetry.

4.2. Open system
A realistic implementation of a strongly-correlated light–matter system should consider the system-bath interaction which leads to loss mechanisms in the initial state preparation and along the dynamics, e.g. if we

consider a experimental realization based on superconducting circuits [15, 17]. In these experiments, the dissipative dynamics is described by a Markovian Lindblad master equation ($\hbar = 1$)

$$\frac{d\rho}{dt} = -i[H_{JCH}, \rho] + \sum_{i=1}^{L}(\gamma\mathbb{L}[\sigma_i^-]\rho + \gamma_\phi\mathbb{L}[\sigma_i^z]\rho + \kappa\mathbb{L}[a_i]\rho), \tag{12}$$

where the Liouvillian operator reads $\mathbb{L}[\mathcal{O}]\rho = \mathcal{O}\rho\mathcal{O}^\dagger - \frac{1}{2}\{\mathcal{O}^\dagger\mathcal{O}, \rho\}$. We consider the same loss mechanisms for each lattice site including energy relaxation, dephasing; and photon losses at rates γ, γ_ϕ, and κ, respectively.

In order to prepare the initial state, we propose to include an ancillary TLS on each lattice site, which interacts with the cavity mode. In this case, the Hamiltonian describing a single lattice site reads

$$H_i = H_{JC}^i + \omega_A\sigma_{A_i}^+\sigma_{A_i}^- + g_A(\sigma_{A_i}^+a_i + \sigma_{A_i}^-a_i^\dagger), \tag{13}$$

where ω_A is the ancilla frequency, g_A the ancilla-cavity coupling strength, and H_{JC}^i the JC Hamiltonian of site i.

The initialization protocol makes use of Gaussian and Stark pulses as described in [76]. First, we let the system to cold down to its ground state $|\psi_0\rangle = \bigotimes_{i=1}^{L}|0, -\rangle_i|\downarrow\rangle_{A_i}$. Second, we apply individual Gaussian π pulses acting upon each ancilla TLS in order to prepare the state $\bigotimes_{i=1}^{L}|0, -\rangle_i|\uparrow\rangle_{A_i}$. Third, a Stark pulse is applied to each ancilla TLS bringing it into resonance with its respective lattice site, i.e. $\omega_A = E_1^-$, during a time interval $\Delta\tau = \pi/(2g_At_1^{--})$. In this way, the strong lattice site-ancilla interaction governed by equation (13) yields the desired initial state $|\psi_0\rangle = \bigotimes_{i=1}^{L}|1, -\rangle_i|\downarrow\rangle_{A_i}$. Notice that one should satisfy the condition $|E_1^+ - E_1^-| \gg g_A$. The latter avoids unwanted population of the state $\bigotimes_{i=1}^{L}|1, +\rangle_i|\downarrow\rangle_{A_i}$. Then, the ancilla-site interaction is suppress by applying a Stark pulse tuning ω_A below the frequency E_1^-. We stress that Stark pulses can be implemented by means of external magnetic fluxes applied upon superconducting quantum interference devices that form a transmon qubit [77, 78].
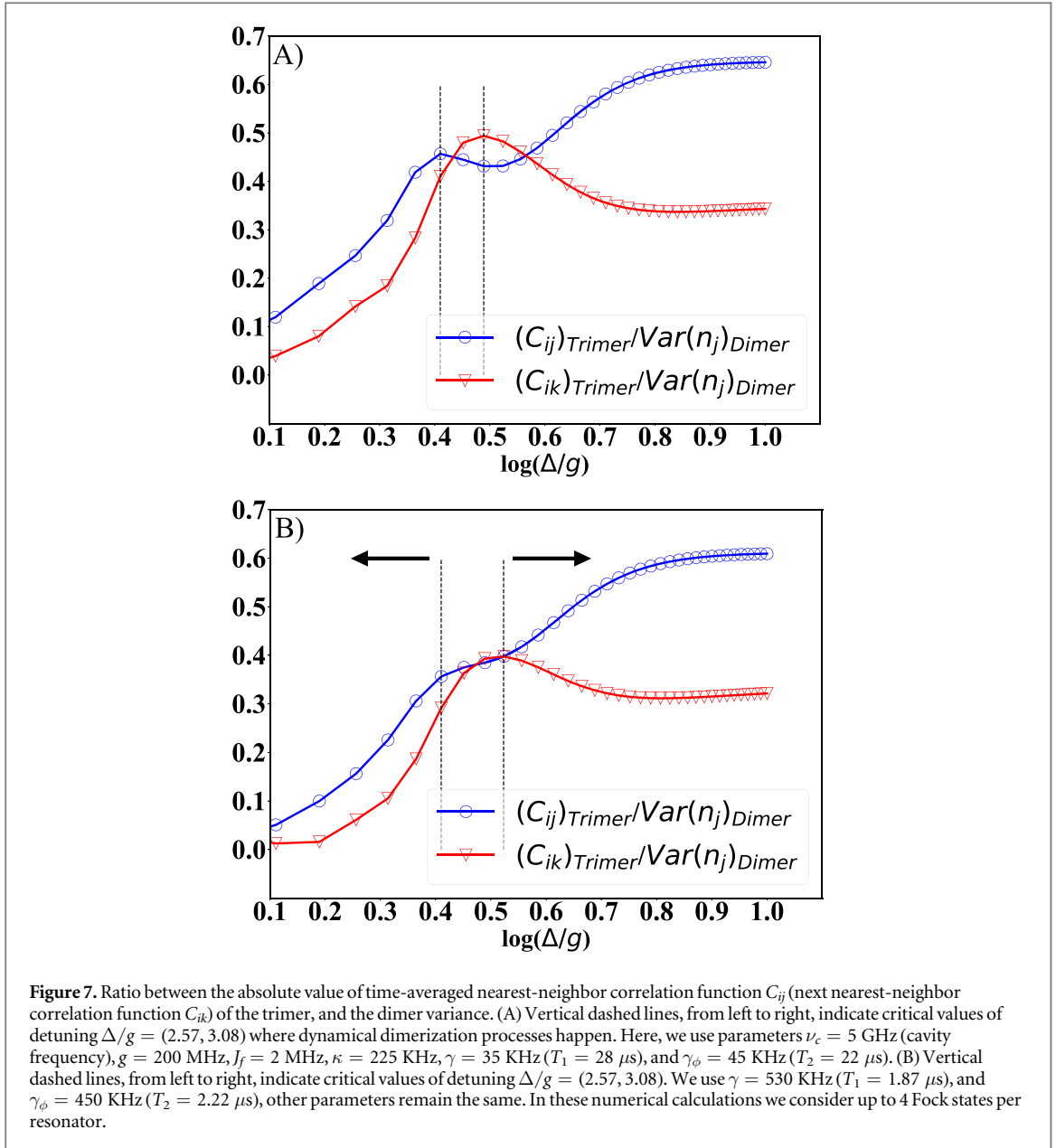
We have numerically calculated the initial state preparation and the sudden quench using the equation (12), using physical parameters taken from state-of-the-art circuit QED setups [15, 17, 78, 79]. Figures 7(a), (b) shows the ratio $(C_{ij})_{Trimer}/Var(n_j)_{Dimer}$ as a function of Δ/g, where $(C_{ij})_{Trimer}$ stands for the absolute value of the time-averaged correlation function, and $Var(n_j)_{Dimer}$ corresponds to the variance of the dimer. As seen in figure 7(a), we identify resonances corresponding to the critical values $\Delta/g = (2.57, 3.08)$, vertical dashed lines, within the intermediate regime of light–matter interaction, $1 < \Delta/g < 10$. In the same way, as in the closed system dynamics 4.1, the trimer experiences dynamical dimerization processes, where short- and long-range correlations dominate over dissipation. As we increase the energy relaxation and dephasing rates of TLSs, resonance peaks are spreading throughout to a wider detuning range, see figure 7(b). These results show evidence about the stability of dynamical dimerization processes that happen in a finite-sized JC lattice, and allow us to establish a parameter threshold for the appearance of DDP in the dissipative case.

In the numerical calculations we use $\nu_c = 5$ GHz (cavity frequency), $g = 200$ MHz, $J_f = 2$ MHz, $\kappa = 225$ KHz, $\gamma = 35$ KHz ($T_1 = 28\,\mu s$), and $\gamma_\phi = 45$ KHz ($T_2 = 22\,\mu s$) [79] for figure 7(a), and $\gamma = 530$ KHz ($T_1 = 1.87\,\mu s$), and $\gamma_\phi = 450$ KHz ($T_2 = 2.22\,\mu s$) [78] for figure 7(b).

5. Conclusions

In summary, we have reported on the emergence of a DDP in a finite-sized JC lattice as a result of a quantum quench from an initial state with integer filling factor. We have thoroughly analyzed the quench dynamics in a close two-sites JC lattice, which allows us to obtain analytical results for time-averaged order parameters such as the local variance of the number of polaritons, and the linear entropy. Further, these order parameters can be used to analyze and predict the resulting quenched dynamics for more complex architectures. When comparing the dimer variance with two-point correlation functions of the trimer and tetramer, it allows us to determine critical values for the detuning where dynamical dimerization processes happen. Recognizing resonances and anti-resonance for detuning values, in turn, allow controlling what kind of correlation dominates over the dynamics be short-range or a combination of both short- and long-range, and may also allow controlling polariton propagation along the lattice. We stress that the intrinsic dimer dynamics, characterized by the time-averaged variance (6), governs the quench dynamics of closed finite-sized JC lattices, and we expect similar results as one increases the number of lattice sites.

In a realistic situation, it is necessary to include dissipative mechanisms in the state preparation and over the quench dynamics. Considering parameters of state-of-the-art circuit QED technology, permit numerical results to show that as one increases the coherence times of TLSs and cavities, two sharp resonance peaks become more evident. These results demonstrate that DDP remains in the dissipative case. We conjecture that for a finite one-dimensional JC lattice of L sites, the number of resonances associated with dimerization processes corresponds to the number of different connectivities of the lattice, that is, connectivity $\nu = 1$ for lattice edges, and connectivity $\nu = 2$ for bulk lattice sites. Our findings could be tested with state-of-the-art quantum

Figure 7. Ratio between the absolute value of time-averaged nearest-neighbor correlation function C_{ij} (next nearest-neighbor correlation function C_{ik}) of the trimer, and the dimer variance. (A) Vertical dashed lines, from left to right, indicate critical values of detuning $\Delta/g = (2.57, 3.08)$ where dynamical dimerization processes happen. Here, we use parameters $\nu_c = 5$ GHz (cavity frequency), $g = 200$ MHz, $J_f = 2$ MHz, $\kappa = 225$ KHz, $\gamma = 35$ KHz ($T_1 = 28$ μs), and $\gamma_\phi = 45$ KHz ($T_2 = 22$ μs). (B) Vertical dashed lines, from left to right, indicate critical values of detuning $\Delta/g = (2.57, 3.08)$. We use $\gamma = 530$ KHz ($T_1 = 1.87$ μs), and $\gamma_\phi = 450$ KHz ($T_2 = 2.22$ μs), other parameters remain the same. In these numerical calculations we consider up to 4 Fock states per resonator.

technologies. For instance, in trapped ions technology, the JCH model has been theoretically proposed in [33] and physically implemented in [34]. In superconducting circuits, the JC dimer has been implemented in [15]. In this case, homodyne signal detection may allow measuring the local variance of photon number, which can also be used as an order parameter.

Acknowledgments

ORCID iDs

Guillermo Romero https://orcid.org/0000-0003-2917-7814

References

[1] Dang L S, Heger D, André R, Bœuf F and Romestain R 1998 Stimulation of polariton photoluminescence in semiconductor microcavity *Phys. Rev. Lett.* **81** 3920–3

[2] Senellart P, Bloch J, Sermage B and Marzin J Y 2000 Microcavity polariton depopulation as evidence for stimulated scattering *Phys. Rev. B* **62** R16263–6

[3] Porras D, Ciuti C, Baumberg J J and Tejedor C 2002 Polariton dynamics and Bose-Einstein condensation in semiconductor microcavities *Phys. Rev. B* **66** 085304

[4] Malpuech G, Di Carlo A, Kavokin A, Baumberg J J, Zamfirescu M and Lugli P 2002 Room-temperature polariton lasers based on GaN microcavities *Appl. Phys. Lett.* **81** 412–4

[5] Kasprzak J *et al* 2006 Bose-Einstein condensation of exciton polaritons *Nature* **443** 409–14

[6] Savvidis P G, Baumberg J J, Stevenson R M, Skolnick M S, Whittaker D M and Roberts J S 2000 Angle-resonant stimulated polariton amplifier *Phys. Rev. Lett.* **84** 1547–50

[7] Ciuti C, Schwendimann P, Deveaud B and Quattropani A 2000 Theory of the angle-resonant polariton amplifier *Phys. Rev. B* **62** R4825–8

[8] Saba M *et al* 2001 High-temperature ultrafast polariton parametric amplification in semiconductor microcavities *Nature* **414** 731–5

[9] Carusotto I and Ciuti C 2004 Probing microcavity polariton superfluidity through resonant rayleigh scattering *Phys. Rev. Lett.* **93** 166401

[10] Kavokin A, Malpuech G and Laussy F P 2003 Polariton laser and polariton superfluidity in microcavities *Phys. Lett. A* **306** 187–99

[11] Tsintzos S I, Pelekanos N T, Konstantinidis G, Hatzopoulos Z and Savvidis P G 2008 A gaas polariton light-emitting diode operating near room temperature *Nature* **453** 372–5

[12] Nunnenkamp A, Koch J and Girvin S M 2011 Synthetic gauge fields and homodyne transmission in Jaynes–Cummings lattices *New J. Phys.* **13** 095008

[13] Houck A A, Türeci H E and Koch J 2012 On-chip quantum simulation with superconducting circuits *Nat. Phys.* **8** 292–9

[14] Underwood D L, Shanks W E, Koch J and Houck A A 2012 Low-disorder microwave cavity lattices for quantum simulation with photons *Phys. Rev. A* **86** 023837

[15] Raftery J, Sadri D, Schmidt S, Türeci H E and Houck A A 2014 Observation of a dissipation-induced classical to quantum transition *Phys. Rev. X* **4** 031043

[16] Underwood D L, Shanks W E, Li A C Y, Ateshian L, Koch J and Houck A A 2016 Imaging photon lattice states by scanning defect microscopy *Phys. Rev. X* **6** 021044

[17] Fitzpatrick M, Sundaresan N M, Li A C Y, Koch J and Houck A A 2017 Observation of a dissipative phase transition in a one-dimensional circuit QED lattice *Phys. Rev. X* **7** 011016

[18] Vaneph C, Morvan A, Aiello G, Féchant M, Aprili M, Gabelli J and Estève J 2018 Observation of the unconventional photon blockade in the microwave domain *Phys. Rev. Lett.* **121** 043602

[19] Ma R, Saxberg B, Owens C, Leung N, Lu Y, Simon J and Schuster D I 2019 A dissipatively stabilized Mott insulator of photons *Nature* **566** 51–7

[20] Collodo M C, Potoč A, Gasparinetti S, Besse J-C, Pechal M, Sameti M, Hartmann M J, Wallraff A and Eichler C 2019 Observation of the crossover from photon ordering to delocalization in tunably coupled resonators *Phys. Rev. Lett.* **122** 183601

[21] Yanay Y, Braumüller J, Gustavsson S, Oliver W D and Tahan C 2019 Realizing the two-dimensional hard-core bose-hubbard model with superconducting qubits arXiv:1910.00933 [quant-ph]

[22] Roushan P *et al* 2017 Spectroscopic signatures of localization with interacting photons in superconducting qubits *Science* **358** 1175–9

[23] Angelakis D G, Santos M F and Bose S 2007 Photon-blockade-induced mott transitions and *XY* spin models in coupled cavity arrays *Phys. Rev. A* **76** 031805

[24] Hartmann M J, Brandao F G S L and Plenio M B 2006 Strongly interacting polaritons in coupled arrays of cavities *Nat. Phys.* **2** 849–55

[25] Greentree A D, Tahan C, Cole J H and Hollenberg L C L 2006 Quantum phase transitions of light *Nat. Phys.* **2** 856–61

[26] Na N, Utsunomiya S, Tian L and Yamamoto Y 2008 Strongly correlated polaritons in a two-dimensional array of photonic crystal microcavities *Phys. Rev. A* **77** 031803

[27] Koch J and Hur K Le 2009 Superfluid-Mott-insulator transition of light in the Jaynes–Cummings lattice *Phys. Rev. A* **80** 023811

[28] Quach J, Makin M I, Su C-H, Greentree A D and Hollenberg L C L 2009 Band structure, phase transitions, and semiconductor analogs in one-dimensional solid light systems *Phys. Rev. A* **80** 063838

[29] Quach J Q, Su C-H, Martin A M, Greentree A D and Hollenberg L C L 2011 Reconfigurable quantum metamaterials *Opt. Express* **19** 11018–33

[30] Halu A, Garnerone S, Vezzani A and Bianconi G 2013 Phase transition of light on complex quantum networks *Phys. Rev. E* **87** 022104

[31] Figueroa J, Rogan J, Valdivia J A, Kiwi M, Romero G and Torres F 2018 Nucleation of superfluid-light domains in a quenched dynamics *Sci. Rep.* **8** 12766

[32] Coto R, Orszag M and Eremeev V 2015 Self-trapping triggered by losses in cavity qed *Phys. Rev. A* **91** 043841

[33] Ivanov P A, Ivanov S S, Vitanov N V, Mering A, Fleischhauer M and Singer K 2009 Simulation of a quantum phase transition of polaritons with trapped ions *Phys. Rev. A* **80** 060301

[34] Toyoda K, Matsuno Y, Noguchi A, Haze S and Urabe S 2013 Experimental realization of a quantum phase transition of polaritonic excitations *Phys. Rev. Lett.* **111** 160501

[35] Jaynes E T and Cummings F W 1963 Comparison of quantum and semiclassical radiation theories with application to the beam maser *Proc. IEEE* **51** 89–109

[36] Fisher M P A, Weichman P B, Grinstein G and Fisher D S 1989 Boson localization and the superfluid-insulator transition *Phys. Rev. B* **40** 546–70

[37] Schmidt S and Blatter G 2009 Strong coupling theory for the Jaynes–Cummings–Hubbard model *Phys. Rev. Lett.* **103** 086403

[38] Rossini D and Fazio R 2007 Mott-insulating and glassy phases of polaritons in 1d arrays of coupled cavities *Phys. Rev. Lett.* **99** 186401

[39] Rossini D, Fazio R and Santoro G 2008 Photon and polariton fluctuations in arrays of QED-cavities *Europhys. Lett.* **83** 47011

[40] D'Souza A G, Sanders B C and Feder D L 2013 Fermionized photons in the ground state of one-dimensional coupled cavities *Phys. Rev. A* **88** 063801

[41] Xue J, Seo K, Tian L and Xiang T 2017 Quantum phase transition in a multiconnected Jaynes–Cummings lattice *Phys. Rev. B* **96** 174502

[42] Grujic T, Clark S R, Jaksch D and Angelakis D G 2012 Non-equilibrium many-body effects in driven nonlinear resonator arrays *New J. Phys.* **14** 103025

[43] Vidal G 2004 Efficient simulation of one-dimensional quantum many-body systems *Phys. Rev. Lett.* **93** 040502

[44] Zwolak M and Vidal G 2004 Mixed-state dynamics in one-dimensional quantum lattice systems: a time-dependent superoperator renormalization algorithm *Phys. Rev. Lett.* **93** 207205

[45] Ogden C D, Irish E K and Kim M S 2008 Dynamics in a coupled-cavity array *Phys. Rev.* A **78** 063805

[46] Makin M I, Cole J H, Hill C D, Greentree A D and Hollenberg L C L 2009 Time evolution of the one-dimensional Jaynes–Cummings–Hubbard Hamiltonian *Phys. Rev.* A **80** 043842

[47] Chakrabarti R and Sreekumari G 2011 Propagation of single-excitation quantum states through Jaynes–Cummings–Hubbard arrays *J. Phys. B: At. Mol. Opt. Phys.* **44** 115505

[48] Coto R and Orszag M 2013 Propagation and distribution of quantum correlations in a cavity QED network *J. Phys. B: At. Mol. Opt. Phys.* **46** 175503

[49] Quach J Q 2013 Disorder-correlation-frequency-controlled diffusion in the Jaynes–Cummings–Hubbard model *Phys. Rev.* A **88** 053843

[50] Johansson J R, Nation P D and Nori F 2012 QuTiP: an open-source Python framework for the dynamics of open quantum systems *Comput. Phys. Commun.* **183** 1760–72

[51] Johansson J R, Nation P D and Nori F 2013 QuTiP 2: a Python framework for the dynamics of open quantum systems *Comput. Phys. Commun.* **184** 1234–40

[52] Benenti G, Casati G, Rossini D and Strini G 2018 *Principles of Quantum Computation and Information* (Singapore: World Scientific) (https://worldscientific.com/doi/pdf/10.1142/10909)

[53] Heyl M 2018 Dynamical quantum phase transitions: a review *Rep. Prog. Phys.* **81** 054001

[54] Heyl M 2019 Dynamical quantum phase transitions: a brief survey *Europhys. Lett.* **125** 26001

[55] Heyl M, Polkovnikov A and Kehrein S 2013 Dynamical quantum phase transitions in the transverse-field Ising model *Phys. Rev. Lett.* **110** 135704

[56] Žunkovič B, Heyl M, Knap M and Silva A 2018 Dynamical quantum phase transitions in spin chains with long-range interactions: merging different concepts of nonequilibrium criticality *Phys. Rev. Lett.* **120** 130601

[57] Halimeh J C and Zauner-Stauber V 2017 Dynamical phase diagram of quantum spin chains with long-range interactions *Phys. Rev.* B **96** 134427

[58] Zauner-Stauber V and Halimeh J C 2017 Probing the anomalous dynamical phase in long-range quantum spin chains through fisher-zero lines *Phys. Rev.* E **96** 062118

[59] Homrighausen I, Abeling N O, Zauner-Stauber V and Halimeh J C 2017 Anomalous dynamical phase in quantum spin chains with long-range interactions *Phys. Rev.* B **96** 104436

[60] Lang J, Frank B and Halimeh J C 2018a Concurrence of dynamical phase transitions at finite temperature in the fully connected transverse-field Ising model *Phys. Rev.* B **97** 174401

[61] Halimeh J C, Van Damme M, Zauner-Stauber V and Vanderstraeten L 2018 Quasiparticle origin of dynamical quantum phase transitions arXiv:1810.07187 [cond-mat.str-el]

[62] Moeckel M and Kehrein S 2008 Interaction quench in the Hubbard model *Phys. Rev. Lett.* **100** 175702

[63] Moeckel M and Kehrein S 2010 Crossover from adiabatic to sudden interaction quenches in the hubbard model: prethermalization and non-equilibrium dynamics *New J. Phys.* **12** 055016

[64] Sciolla B and Biroli G 2010 Quantum quenches and off-equilibrium dynamical transition in the infinite-dimensional Bose-Hubbard model *Phys. Rev. Lett.* **105** 220401

[65] Gambassi A and Calabrese P 2011 Quantum quenches as classical critical films *Europhys. Lett.* **95** 66007

[66] Sciolla B and Biroli G 2013 Quantum quenches, dynamical transitions, and off-equilibrium quantum criticality *Phys. Rev.* B **88** 201110

[67] Maraga A, Chiocchetta A, Mitra A and Gambassi A 2015 Aging and coarsening in isolated quantum systems after a quench: exact results for the quantum (n) model with n *rightarrow infty Phys. Rev.* E **92** 042151

[68] Mori T, Ikeda T N, Kaminishi E and Ueda M 2018 Thermalization and prethermalization in isolated quantum systems: a theoretical overview *J. Phys. B: At. Mol. Opt. Phys.* **51** 112001

[69] Zhang J, Pagano G, Hess P W, Kyprianidis A, Becker P, Kaplan H, Gorshkov A V, Gong Z X and Monroe C 2017 Observation of a many-body dynamical phase transition with a 53-qubit quantum simulator *Nature* **551** 601

[70] Halimeh J C, Zauner-Stauber V, McCulloch I P, de Vega I, Schollwöck U and Kastner M 2017 Prethermalization and persistent order in the absence of a thermal phase transition *Phys. Rev.* B **95** 024302

[71] Karrasch C and Schuricht D 2013 Dynamical phase transitions after quenches in nonintegrable models *Phys. Rev.* B **87** 195104

[72] Andraschko F and Sirker J 2014 Dynamical quantum phase transitions and the loschmidt echo: a transfer matrix approach *Phys. Rev.* B **89** 125120

[73] Jurcevic P, Shen H, Hauke P, Maier C, Brydges T, Hempel C, Lanyon B P, Heyl M, Blatt R and Roos C F 2017 Direct observation of dynamical quantum phase transitions in an interacting many-body system *Phys. Rev. Lett.* **119** 080501

[74] Piroli L, Pozsgay B and Vernier E 2018 Non-analytic behavior of the Loschmidt echo in XXZ spin chains: exact results *Nucl. Phys.* B **933** 454–81

[75] Lang J, Frank B and Halimeh J C 2018 Dynamical quantum phase transitions: a geometric picture *Phys. Rev. Lett* **121** 130603

[76] Majer J *et al* 2007 Coupling superconducting qubits via a cavity bus *Nature* **449** 443–7

[77] Koch J, Yu T M, Gambetta J, Houck A A, Schuster D I, Majer J, Blais A, Devoret M H, Girvin S M and Schoelkopf R J 2007 Charge-insensitive qubit design derived from the Cooper pair box *Phys. Rev.* A **76** 042319

[78] Schreier J A *et al* 2008 Suppressing charge noise decoherence in superconducting charge qubits *Phys. Rev.* B **77** 180502

[79] Chow J M, Srinivasan S J, Magesan E, Córcoles A D, Abraham D W, Gambetta J M and Steffen M 2015 Characterizing a four-qubit planar lattice for arbitrary error detection *SPIE* **9500** 315–23